Carbon-supported Fe catalysts with well-defined active sites for highly selective alcohol production from Fischer-Tropsch synthesis

Yanping Chen [a,1], Lixuan Ma [c], Riguang Zhang [c], Runping Ye [a], Wei Liu [a], Jiatong Wei [a], Vitaly V. Ordomsky [b,*,2], Jian Liu [a,d,**,3]

[a] State Key Laboratory of Catalysis, Dalian Institute of Chemical Physics, Chinese Academy of Sciences, 457 Zhongshan Road, Dalian 116023, Liaoning, China
[b] UMR 8181 – UCCS – Unité de Catalyse et Chimie du Solide, Univ. Lille, CNRS, Centrale Lille, ENSCL, Univ. Artois, F-59000 Lille, France
[c] State Key Laboratory of Clean and Efficient Coal Utilization, Key Laboratory of Coal Science and Technology, Taiyuan University of Technology, Taiyuan 030024, Shanxi, China
[d] DICP-Surrey Joint Centre for Future Materials, Department of Chemical and Process Engineering, and Advanced Technology Institute, University of Surrey, Guildford, Surrey GU2 7XH, UK

ARTICLE INFO

ABSTRACT

Alcohols are important chemicals, and are considered as high value-added products from Fischer–Tropsch synthesis (FTS). However, the unknown active sites and their unclear alcohol formation mechanism hinder the development of highly efficient catalysts. Herein, we report the design of low cost and scalable carbon-supported Fe (K-Fe/NC) catalyst with tailorable FTS selectivity via pyrolysis of Prussian Blue. Our K-Fe/NC catalyst exhibits alcohol selectivity as high as 30% containing 95% of C_2-C_{13} fraction. The K-Fe/NC catalyst with a core-shell structure facilitates the investigation of iron structural evolution in FTS. The CO dissociation and association are thoroughly verified through theoretical calculations and the temperature-programmed surface reaction of CO. The synergistic effect between χ–Fe_5C_2/ε-Fe_2C and Fe_3O_4 dual active sites is proposed for the alcohol formation mechanism. This work provides significant insight into the development of low cost and highly efficient iron-based catalysts for alcohols in FTS.

1. Introduction

Fischer–Tropsch synthesis (FTS) has been widely applied in industry for the conversion of coal, natural gas, and biomass into hydrocarbons and oxygenates. The FTS technology is desirable for the development of low cost and more efficient catalysts to produce high value-added clean and environmentally friendly products (lower olefins, α-olefins, alcohols, and other oxygenates) from renewable feedstocks [1,2]. Higher alcohols are industrial raw chemicals for detergent [3]. Compared with cobalt catalysts, the precipitated iron catalysts are economically attractive and highly abundant with relatively high selectivity towards alcohols. However, the precipitated iron catalysts undergo complex phase and structural evolution under FTS conditions due to the

carbonization of iron particles resulting in carbon deposition and fragmentation [4,5]. The complex structural evolution of the iron particles further hinders the identification of the active sites for the formation of alcohol products in FTS. Therefore, a deep understanding of the structural evolution of iron particles is crucial for the improvement of alcohol selectivity in FTS.

The traditional precipitated iron catalysts have been largely investigated to confirm the phase and structure evolution of iron particles. However, many factors hinder this investigation, for example: 1) the bulk precipitated iron catalysts undergo various carbonization degrees; 2) the residual iron oxides after reduction and carbonization may deposit onto the regenerated iron oxides during the reaction, confusing the real structure and phase evolution [6–8]. It was confirmed that the iron

---

carbides are formed mainly beside and outside the Fe_3O_4 particle [9–11]. The investigation of iron evolution is impeded by the carbon deposition-induced fragmentation and the sintering-induced aggregation of iron particles. Shroff et al. observed that magnetite crystals were broken down into smaller crystallites of iron carbide phase due to the carbon deposition [12]. Ding et al. found that, during the carbonization process, the precipitated iron catalyst was firstly reduced from α-Fe_2O_3 to Fe_3O_4, accompanied simultaneously by the formation of atomic, polymeric and graphitic-type carbonaceous species on the surface of the catalyst [13,14]. Davis et al. found that the iron particles of the spent precipitated iron catalyst are with a multi-shell structure as A@B@C [15]. The core of A is an iron carbide particle, the inner shell of B is composed of an iron oxide phase, and the outer shell of C is deposited carbon. So far, many debates about the structure and phase evolution of iron particles in FTS are in the literature, which impedes the identification of active phases. Therefore, it is necessary to design iron catalysts with stable and uniformly distributed iron particles for investigating the structure and phase evolution of the iron particles in FTS.

Currently, various bimetallic iron catalysts have been reported in the literature for the alcohol product in FTS, such as FeCu [16], FeRh [17], FeMo [18], etc. Taking the FeCu catalyst as an example, the synergistic effect of iron carbides and copper dual sites are considered as the active centers for alcohol formation [16]. Monometallic iron catalysts have also been demonstrated for considerable alcohol selectivity compared with bimetallic iron catalysts [19]. However, the alcohol selectivity over monometallic iron catalysts is very low and there is less discussion about their formation mechanism. It is meaningful to investigate the formation mechanism of the alcohol product on the monometallic iron catalysts and improve the alcohol selectivity in FTS.

Herein, we prepared carbon supported iron (K-Fe/NC) catalysts through the pyrolysis of Prussian Blue (PB, $Fe_4^{III}[Fe^{II}(CN)_6]_3$) coordination polymer for alcohols of FTS. The K-Fe/NC catalyst presents uniformly distributed iron particles confined in the carbon matrix which benefits the investigation of the iron nanoparticle evolution. The in situ activation and structural and phase evolution of iron nanoparticles during FTS process was confirmed. The chemical adsorption and surface reaction techniques and theoretical calculations were applied to investigate the alcohol formation mechanism.

2. Experimental

2.1. Materials

Ferric nitrate nonahydrate ($Fe(NO_3)_3.9H_2O$), ferrous sulfate heptahydrate ($FeSO_4.7H_2O$), potassium hexacyanoferrate (III) ($K_3Fe(CN)_6$), and trisodium citrate dihydrate ($Na_3C_6H_5O_7 \cdot 2H_2O$) were purchased from Sinopharm Chemical Reagent Co., Ltd, Silicon dioxide (SiO_2, BET surface area $= 300 \, m^2/g$ and particle size $= 30$–60 mesh) was purchased from Aladdin company. All chemical reagents were analytical grade and used without any treatment. Deionized water (DI) was used in all the above experiments. Washing was done with deionized water and reagent-grade ethanol.

2.2. Synthesis of PB

PB as precursors for the subsequent experiments was prepared by a simple precipitation method, as reported in the literature [20]. Firstly, solution A was obtained by adding 0.6 mmol of $FeSO_4.6H_2O$ and 0.9 mmol of $Na_3C_6H_5O_7 \cdot 2H_2O$ into 20 ml of deionized water. Secondly, solution B was obtained by adding 0.4 mmol of $K_3Fe(CN)_6$ into 20 ml of deionized water. Thirdly, solution B was added slowly into solution A under vigorous and continuously stirring, and then the obtained mixture was aged at room temperature for 24 h. Finally, the aged mixture was treated by centrifugation, washing with water and ethanol, and drying at 60 °C overnight. The PB powder was obtained.

2.3. Synthesis of K-Fe/NC-fresh-P catalyst

The as-prepared PB powder was further pyrolyzed at 500 °C for 4 h with a heating rate of 3 °C min^{-1} under a flow of N_2 atmosphere. After the pyrolysis process, the temperature was decreased to room temperature under N_2 atmosphere, and then the N_2 was changed to air for the passivation of the K-Fe/NC catalyst. Finally, the K-Fe/NC-fresh-P catalyst was obtained. Particularly, the K-Fe/NC-fresh and K-Fe/NC-fresh-P catalyst were denoted as the freshly prepared K-Fe/NC catalyst without and with air passivation respectively. The reference 15Fe/SiO$_2$ catalyst was prepared by the incipient-wetness impregnation method. 1.09 g Fe (NO_3)$_3$.9 H_2O was dissolved in 3.00 g DI water, and 0.85 g SiO_2 was impregnated repeatedly by the above solution. After drying, the subsequent calcination was carried out at 450 °C for 4 h with a heating rate of 3 °C min^{-1} under a flow of air atmosphere.

2.4. Catalyst characterization

A Rigaku D/Max2500PC diffractometer with Cu Kα radiation ($\lambda = 1.5418$ Å) was used to perform powder X-ray diffraction (XRD) at room temperature in the 2θ range of 5–80° (5° min^{-1}). *In situ* XRD was performed with the temperature-programmed process in N_2 with a heating rate of 5° min^{-1}. The temperature and 2θ range were 30–400 °C and 10–70° respectively. The transmission electron microscopy (TEM) images were recorded with a FEI Tecnai G^2 Spirit microscope operated at 120 kV. The high-resolution transmission electron microscopy (HRTEM) images were taken using a FEI Tecnai G^2 F30S-Twin microscope operated at 300 kV. The elemental mapping was tested on a JEM ARM200F thermal-field emission microscope with a probe spherical aberration (*Cs*) corrector at 200 kV. A convergence angle of ~23 mrad and a collection angle range of 68–174 mrad were adapted for the high-angle annular dark-field scanning transmission electron microscopy (HAADF-STEM) imaging. For the TEM sample preparation, the sample was dispersed in ethanol and dropped onto the copper grids and dried on a hot plate for a while (80 °C). The temperature-programmed desorption of CO (CO-TPD) was carried out on a Micromeritics Autochem II 2920 chemisorption apparatus. For the sample with CO-0.3 h pretreatment, 0.1 g of the K-Fe/NC-fresh-P catalyst was firstly pretreated at 240 °C under 10% CO /He (balanced by He) (30 ml min^{-1}) for 0.3 h. The temperature was decreased to 50 °C in He and then the sample was exposed to 10% CO/He at 50 °C for 1 h. After purging in He for 1 h, the sample with adsorbed CO underwent the temperature-programmed desorption of CO from 50° to 700°C and the desorbed gas was monitored by a mass spectrometer (MS). Similarly, the samples with CO-2 h pretreatment, CO$_2$-2 h pretreatment, and syngas-2 h (H$_2$/CO=2) pretreatment were performed as that the K-Fe/NC-fresh-P catalysts were pretreated with CO, CO$_2$, and syngas at 240 °C for 2 h. The sample with H$_2$-2 h pretreatment was performed as that the K-Fe/NC-fresh-P catalysts were pretreated with H$_2$ at 400 °C for 2 h. The subsequent CO-TPD followed the same procedure with the CO-0.3 h pretreatment sample. The sample without pretreatment was performed as the K-Fe/NC-fresh-P catalyst without any pretreatment underwent the temperature-programmed desorption in He from 50° to 700°C. The temperature-programmed surface reaction of CO (CO-TPSR) was tested on the same apparatus as CO-TPD. 0.1 g of the K-Fe/NC-fresh-P catalyst was pretreated at 240 °C under 10% CO/He (30 ml min^{-1}) for 0.3 h or 2 h (CO-0.3 h/2 h pretreatment). After the temperature decreased to 50 °C in He, the sample was exposed to 10% CO/He at 50 °C for 1 h. Then He purging was carried out. The purged sample underwent temperature-programmed desorption in 10% H$_2$/He (30 ml min^{-1}) from 50° to 700°C and the desorbed gas was monitored by MS. The room temperature ^{57}Fe Mössbauer spectra were recorded using a proportional counter and a Topologic 500 A spectrometer. A ^{57}Co (Rh), moving with a constant acceleration mode, was used as the γ-ray radioactive source. The velocity was calibrated by a standard a-Fe foil. The spectra were fitted on the base of Lorentzian adsorption curves using MossWinn 3.0i

computer program. The derived hyperfine parameters, such as isomer shift (IS), quadruple splitting (QS), and magnetic hyperfine field (H), were employed for component identification. The phase content was obtained based on the areas of the adsorption peaks, assuming the iron nuclei for all catalysts have the same probability of adsorption of γ photons. Thermogravimetric Analysis (TGA) was performed on a PerkinElmer TGA4000 with nitrogen as a carrier gas. Nitrogen adsorption-desorption data was acquired using a Micromeritics Tristar II 2460 automated analyzer at 77 K. The specific surface area was calculated using the Brunauer-Emmett-Teller (BET) method. Before analysis, the samples were degassed at 120 °C under a vacuum overnight. Raman measurements were obtained by NanoWizard Ultra Speed & inVia Raman spectrometer using the laser with an excitation wavelength of 532 nm. X-ray photoelectron spectroscopy (XPS) was conducted using a KRATOS Axis Ultra[DLD] spectrometer equipped with a monochromated aluminum source (Al Kα = 1486.6 eV) and charge compensation gun. Charge correction with C 1 s = 284.60 eV as the energy standard. Inductively coupled plasma optical emission spectrometry (ICP-OES) was carried out on an ICPS-8100 to confirm the content of the metal. The sample was previously calcined at 600 °C in the air to remove carbon species and then dissolved in acid (An acidic mixture of HNO_3 and HCl). The element analyzer (EMGA-930) was used for the element analysis of O, N, and H. The element analysis of C was confirmed by an Element analyzer (EMIA-8100).

2.5. Catalyst testing

The FTS reaction was carried out in a fixed-bed reactor with an inner diameter of 10 mm and a bed length of 53 cm. 0.50 g of PB precursors (20–40 mesh) and 1.80 g of silica sand were loaded into the reaction tube. Before the reaction, the catalyst was in situ pyrolyzed in nitrogen (30 ml min^{-1}) at 500 °C for 4 h and then cooled to 180 °C. After the pyrolysis, the FTS reactions were carried out at 240 °C, 3 MPa, and a gas hourly space velocity (GHSV) of 4.5 L g_{cat}^{-1} h^{-1} in syngas (H_2/CO = 2). 4% of N_2 in CO was used as a reference gas for calculating CO conversion. The gas products of CO, CO_2, and CH_4 were analyzed by an online gas chromatograph (GC) equipped with a Thermal Conductivity Detector (TCD) and columns of Molecular sieve-13X (80/100 mesh, 3.0 m × 3.2 mm×2.1 mm) and Porapak-N (80/100 mesh, 1.0 m × 3.2 mm × 2.1 mm). The other gas products of CH_4 and C_2-C_4 hydrocarbon were analyzed by the on-line GC with a Flame Ionization Detector (FID) and column of Rt-QPLOT (0.32 mm × 10 μm × 30 m). Liquid products were collected in a cold trap at 2 °C and the liquid oil product of C_5 + hydrocarbons and oxygenates were analyzed on an offline GC equipped with an FID detector and column of Rtx-1 (SH-Rtx-1 3.0 m × 3.2 mm×2.5 mm). The liquid C_1-C_5 oxygenates in the water phase were analyzed by an offline GC with FID detector and a column of SH-Stailwax-DA (3.0 m × 3.2 mm × 2.5 mm). Only trace amounts of oxygenates were detected from water for the $15Fe/SiO_2$ catalyst, hence the oxygenates in the water phase can be ignored. A hot trap of 150 °C was used to collect wax products and there is no wax product for the K-Fe/NC catalyst. The cold trap and the hot trap were operated to collect the product at a time on stream (TOS) of 24 h and 60 h, respectively. The carbon balance of all carbon-containing products was above 93%. After the FTS reaction, the temperature of the reactor was decreased to room temperature under N_2 atmosphere, and then the flow of N_2 was changed to that of air for the passivation of the spent K-Fe/NC catalyst. Finally, the K-Fe/NC-spent-P catalyst was obtained. The CO conversion and product selectivity were calculated according to literature [21], and the equations were listed in the supporting information.

2.6. DFT calculations

2.6.1. Computational methods

Density Functional Theory (DFT) calculations with spin-polarization were applied using the Vienna ab initio simulation package (VASP) [22], the exchange-correlation energies were calculated by the generalized gradient approximation joints to the Perdew–Burke–Ernzerhof (GGA-PBE) functional [23].

2.6.2. Catalyst models

Fe_3O_4 with *Fd-3m* space group corresponds to the lattice constants of 8.390 Å, which agrees with the previous studies (*a=b=c=*8.394 Å) [24, 25]. As shown in Fig. S1a, the unit cell of Fe_3O_4 has an anti-spinel structure $[Fe^{3+}]_{tet}[Fe^{2+}Fe^{3+}]_{oct}O_4^{2-}$, both the tetrahedral (tet) and octahedral (oct) sites are occupied by Fe ions. The hexagonal ε-Fe_2C phases (Fig. S1b) with *P63/mmc* space group have the lattice constants of *a=* 5.486 Å, *b=* 5.647 Å, *c=* 4.284 Å, which is closer to the previous results (*a=*5.472 Å, *b=*5.639 Å, *c=*4.280 Å) [26,27]. The bulk of χ-Fe_5C_2 is the monoclinic phase with C2/c symmetry (Fig. S1c) and the lattice constants of *a* = 11.545 Å, *b* = 4.496 Å, *c* = 4.982 Å, which are consistent with the experimental values of *a* = 11.558 Å, *b* = 4.579 Å, *c* = 5.069 Å [28,29]. The most exposed Fe_3O_4(311), ε-Fe_2C(101) and χ-Fe_5C_2(510) surfaces were chosen as the model catalysts using the *p*(1 ×2), *p*(2 ×2) and *p*(2 ×1) supercell, respectively (see Fig. S1d–f). The detailed structure parameters are summarized in Table S1.

3. Results and discussion

3.1. Catalytic performances

The PB precursor underwent in situ pyrolysis in the fixed-bed reactor and the obtained K-Fe/NC-fresh catalyst has been directly tested in the FTS reaction without air exposure. As shown in Fig. 1A, the CO conversion can be divided into two stages with a decrease of the CO conversion at the beginning of TOS (0–24 h) and further stabilization (24–60 h). At the initial reaction stage, the CO conversion shows a downward trend with an increase of the selectivity to methane and lower olefins with a decrease of the selectivity to C_5+ and oxygenates (Fig. 1D). The K-Fe/NC catalyst demonstrates a higher CO_2 selectivity of 45% in comparison with 15% over impregnated $15Fe/SiO_2$ catalyst. The high CO_2 selectivity of K-Fe/NC catalyst comes from the water gas shift (WGS) reaction (CO + H_2O = CO_2 + H_2), hence there is no water in the products due to the water consumption by WGS. It has to be noted that the carbon number of the oil product is less than 25 over K-Fe/NC catalyst, which is lower than that of the $15Fe/SiO_2$ reference catalyst (Figs. 1B, E, H, S2). There is a much higher amount of C_5 + paraffins for the 0–24 h oil than that of the 24–60 oil. It can be explained by the modification of the catalyst during the first 24 h of the test. For the K-Fe/NC catalyst, the chain growth probability of α values obtained from the Anderson-Schulz-Flory (ASF) distribution is similar with alcohols of 0.62 and 0.61 as well as α-olefins of 0.67 and 0.66 in the 0–24 h and 24–60 h oil product, respectively (Fig. 1C, F). It is supposed that two types of active sites are responsible for the alcohol and paraffin product, and the contribution of the active sites for paraffins generation is decreasing as the reaction proceeds from the initial to the stable stage. The $15Fe/SiO_2$ catalyst exhibits similar α values of α-olefins and slightly higher that of alcohols, compared with K-Fe/NC catalyst (Fig. 1I). The fraction of alcohols produced over K-Fe/NC catalyst at the stable stage contains 5% of methanol, 56% of C_2OH-C_5OH and 39% of C_6OH-C_{13}OH (Fig. 1G).

The traditional precipitated iron catalysts in the previous works exhibited 8–9% oxygenate selectivity, denoting the alcohol selectivity below that value [9,30–32]. The potassium promoter facilitates olefin formation. The Fe time yield (FTY) of K-Fe/NC catalyst is a little lower than that of the impregnated $15Fe/SiO_2$ catalyst and the precipitated iron catalysts from the literature, probably due to the deep carbonization of iron in K-Fe/NC catalyst. The alcohol selectivity of K-Fe/NC-spent-60 h can achieve 30% at the selectivity to lower olefins and linear α-olefins (LAO) 23% and 14%, respectively, which are all much higher than that of the $15Fe/SiO_2$ catalyst and the precipitated iron catalysts reported in the literature (Table 1). The special phase
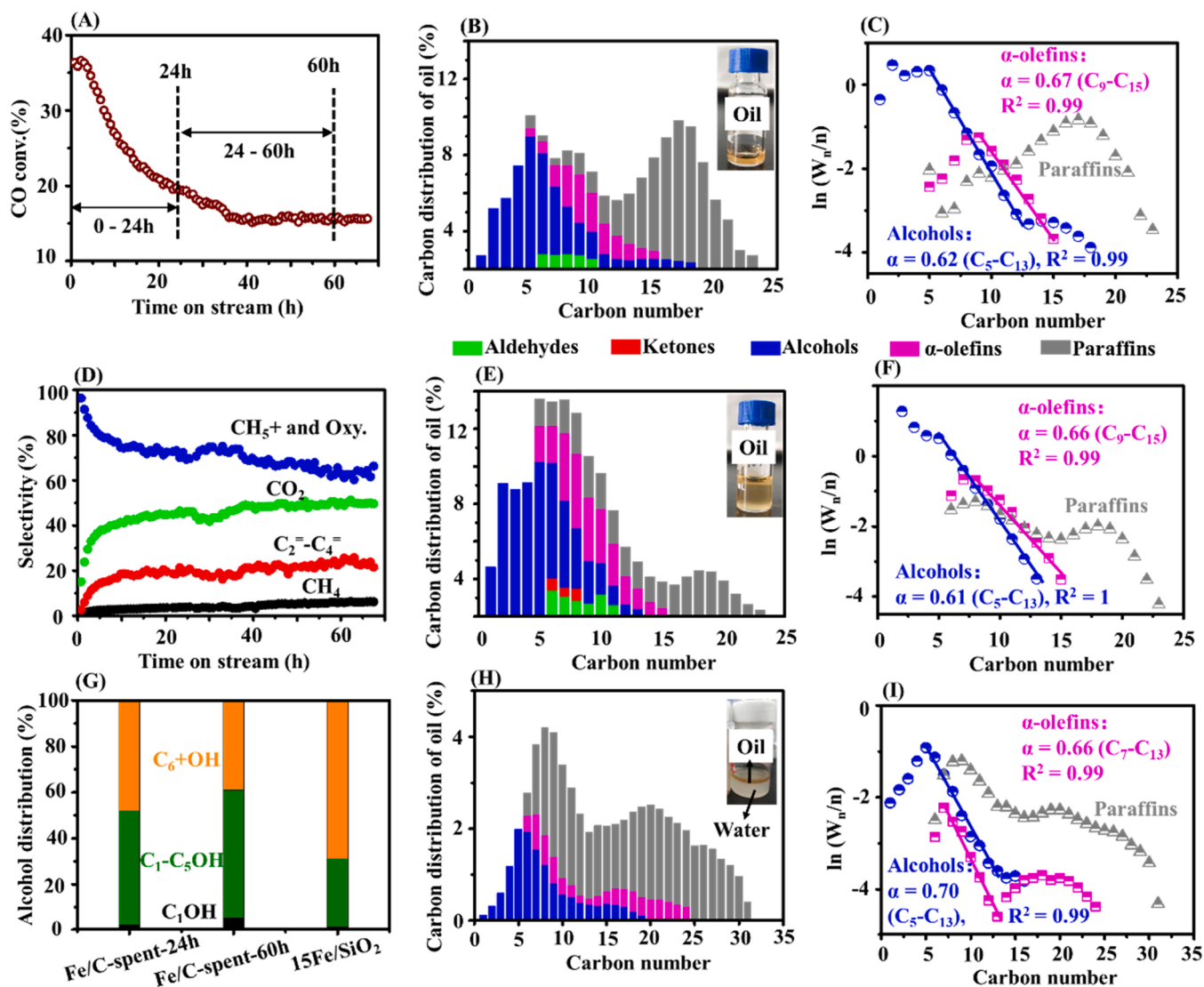
Fig. 1. Catalytic performances. CO conversion vs TOS (A). The carbon number distribution of the oil product collected at TOS of 0–24 h (B) and 24–60 h (E) for the K-Fe/NC catalyst, and the corresponding ASF plots of TOS of 0–24 h (C) and 24–60 h (F). CH_4, $C_{2=}$-$C_{4=}$, C_5+ and Oxy., and CO_2 selectivity vs TOS (D). The alcohol distribution (G). The carbon number distribution of the oil and wax product for the impregnated 15Fe/SiO_2 catalyst (H), and the corresponding ASF plots (I). Aldehydes (green), ketones (red), α-olefins (pink), alcohols (blue), and paraffins (gray). α denotes the carbon chain growth probability. W_n denotes the mass fraction of the product, n denotes the carbon number. CH_5+ and Oxy. denotes hydrocarbons with carbon number above 5 and oxygenates. C_1OH denotes methanol. C_2-C_5OH denotes alcohols with carbon number of 2–5. C_6OH+ denotes alcohols with carbon number above 6.

composition of the K-Fe/NC catalyst contributes to the high alcohol selectivity. The K-Fe/NC-spent-60 h demonstrates lower CH_4 selectivity than the 15Fe/SiO_2 catalyst due to the lower H_2 adsorption in the presence of potassium.

3.2. Catalyst structural investigation

Fig. 2A shows the schematic diagram of the K-Fe/NC-fresh-P preparation through the pyrolysis of PB and the subsequent passivation. PB is an important coordination polymer, in which two different metal centers Fe^{3+} and Fe^{2+} are bridged by the CN^- groups [33,34]. During the pyrolysis process, iron ions may agglomerate into iron carbide/nitride particles, and the CN^- turns into a porous N-doped carbon matrix. The FeC_x/FeN_x @FeO_x core-shell structure is generated via the passivation of FeC_x/FeN_x core in the air. The TEM image shows 50–100 nm of PB particles (Fig. 2C). The pyrolysis of the PB precursor starts at 100 °C, and the surface area is 38.3 m^2/g. The I_D/I_G ratio of Raman spectra is 1.2, indicating a considerable graphitization degree of the K-Fe/NC-fresh-P

catalyst (Fig. S3). XRD patterns demonstrate the disappearance of the PB diffraction peaks and growth of the ε-Fe_2C peaks with an increase of the pyrolysis temperature from 25° to 500°C (Fig. 2B). From Fig. 2D, it is evident that the K-Fe/NC-fresh-P catalyst consists of nanoparticles with sizes of ~20 nm. The HRTEM images demonstrate that all particles present a core-shell structure with a shell thickness of 5 nm (Fig. 2E). The core shows clear lattice fringes with an interplanar distance of 2.01 Å, which can be ascribed to the (101) planes of ε-Fe_2C (Fig. 2F). The shell presents the lattice fringes of Fe_3O_4 (311).

The impregnated 15Fe/SiO_2 presents disordered iron particles distributed in SiO_2 support without clear boundaries (Fig. 3A), which makes it hard to investigate the structural evolution of iron particles. However, the K-Fe/NC-spent-60 h-P catalyst manifests well-distributed iron particles in the carbon matrix with a particle size of ~20 nm (Fig. 3B). The structure and phase evolution of iron particles can be well observed by investigation of the K-Fe/NC catalyst. The HRTEM of K-Fe/NC-spent-60 h-P catalyst presents the core with χ-Fe_5C_2 (510) / ε-Fe_2C (101) lattice fringes and the shell with Fe_3O_4 (311) lattice fringes

Table 1
Catalytic performances of the K-Fe/NC catalyst and the reference catalyst in comparison with the literature.

Catalysts	Metal state			T /°C	CO Conv. (%)[c]	FTY (mmol$_{CO}$ g$_{Fe^{-1}}$ h^{-1})[d]	CO$_2$ sel. (%)[e]	Product selectivity (%)							Ref.
	Fe (wt %)[a]	K (wt %)	Size (nm)[b]					CH$_4$	C$_2$=-C$_4$-[f]	C$_2$o-C$_4$o[g]	C$_5$o+[h]	C$_5$=+[i]	ROH[j]	RO[k]	
K-Fe/NC-spent-24h	61	2	20	240	21	15	45	3	18	4	37	9	27	2	This work
K-Fe/NC-spent-60h					16	11	49	5	23	6	17	14	30	5	
15Fe/SiO$_2$	15	0	15	240	18	26	15	16	15	13	34	7	15	0	
30Fe/SiO$_2$	30	0	15	240	27	40	10	11	12	13	39	8	17	0	
								CH$_4$	C$_2$-C$_4$[l]		C$_5$+[m]		Oxy.[n]		
100Fe	100	0	11	280	35	29	26	18	43		31		8		[31]
100Fe/20SiO$_2$	83	0	14	270	64	23	26	20	43		38		9		[9]
100Fe12Mn1.5K /10SiO$_2$	81	1	2	260	43	9	34	9	31		51		9		[30]
								CH$_4$	C$_2$=-C$_4$-	C$_2$o-C$_4$o	C$_5$o-C$_{11}$o[p]	C$_5$=-C$_{11}$-[o]	C$_{12}$+[q]	Oxy.	
100Fe	100	0		260	75	20	45	8	7.2	3.6	14	12	55	0	[32]
100Fe5K	95	5		260	76	21	46	4	4	1	5	15	71	0	[32]

Reaction condition: 240 °C, 3.0 MPa, H$_2$/CO = 2.0, 4000 h^{-1} (K-Fe/NC), 3000 h^{-1} (15Fe/SiO$_2$). Ref. [31]: 1.5MPa, H$_2$/CO=1.6, 3000h^{-1}, TOS=193h. Ref. [9]: 2MPa, H$_2$/CO=1.5, 2000h^{-1}, TOS=72h. Ref. [30]: 1.5MPa, H$_2$/CO=1.2, 2000h^{-1}, TOS=162h. Ref. [32]: 1.5MPa, H$_2$/CO=0.67, 1000h^{-1}, TOS=97h. Notes: K-Fe/NC-spent-24h and K-Fe/NC-spent-60h samples denote the catalytic data for the TOS of 24h with 0-24h oil, and TOS of 60h with 24-60h oil, respectively. [a] Fe and K content obtained from ICP-OES. [b] Metal size obtained from TEM. [c] CO conv. denotes CO conversion. [d] FTY denotes Iron time yield, the converted CO amount per unit time and unit mass of iron. [e] CO$_2$ sel. denotes CO$_2$ selectivity. [f] C$_2$=-C$_4$= denotes olefins with carbon number of 2-4. [g] C$_2$o-C$_4$o denotes paraffins with carbon number of 2-4. [h] C$_5$o+ denotes paraffins with carbon number above 5. [i] C$_5$=+ denotes α-olefins with carbon number above 5. [j] ROH denotes alcohols. [k] RO denotes aldehydes and ketones. [l] C$_2$-C$_4$ denotes hydrocarbons with carbon number of 2-4. [m] C$_5$+ denotes hydrocarbons with carbon number above 5. [n] Oxy. denotes oxygenates. [o] C$_5$=-C$_{11}$= denotes olefins with carbon number of 5-11. [p] C$_5$o-C$_{11}$o denotes paraffins with carbon number of 5-11. [q] C$_{12}$+ denotes hydrocarbon with carbon number above 12.

(Fig. 3C). HAADF-STEM confirms the core-shell structure of the K-Fe/NC-spent-60 h-P catalyst and the corresponding elemental mapping images present the core is mainly composed of C and Fe while the shell contains O and Fe (Fig. 3D). The element content in the bulk and surface are determined by ICP-OES, element analysis, and XPS (Figs. S4, S5, Table S2). The bulk of the K-Fe/NC-fresh-P catalyst mainly contains Fe, C, O, K, and N elements with Fe accounting for 60.5%. The XPS survey spectrum of the K-Fe/NC catalysts indicates that the surface contains Fe, C, O, K, and N. The surface composition of the K-Fe/NC-fresh-P and the K-Fe/NC-spent-2 h-P catalysts is dominated by O, accounting for 65.2% and 62.8% respectively. Yet K-Fe/NC-spent-60 h-P is dominated by C, accounting for 67.6%, which may be caused by carbon deposition during the FTS reaction. The XPS spectra of the C1s showed that all three samples are mainly C sp^2, accompanied by a small amount of C sp^3. The C sp^2 belongs to the graphitized carbon matrix. The XPS spectra of the O 1 s of K-Fe/NC-fresh-P showed that 45.9% of H$_2$O at a characteristic binding energy peak of 532.5 eV and 54.1% of Fe-OH at 531.6 eV. As shown in Fig. 3E, the XPS spectrum of the Fe 2p region of all three samples can be fitted with two spin-orbit doublets corresponding to the Fe 2p$_{3/2}$ and Fe 2p$_{1/2}$ peaks and the corresponding satellite peaks of Fe^{2+} and Fe^{3+}, which are typical characteristic peaks of Fe$_3$O$_4$ [35]. The Fe$_3$O$_4$ peaks of all three samples are assigned to the iron oxide shell of iron particles in K-Fe/NC catalyst. From Fig. 3F, it can be seen that the fresh and spent K-Fe/NC catalysts demonstrate ε-Fe$_2$C diffraction peaks, with some Fe$_3$O$_4$ peaks emerging (standard XRD patterns, ε-Fe$_2$C: #17-0897, χ-Fe$_5$C$_2$: #51-0997, Fe$_3$O$_4$: #19-0629).

As shown in Fig. 4 (A) and (D), the Mössbauer spectra of K-Fe/NC-fresh-P indicate the coexistence of FeN$_4$, Fe$_x$C, θ-Fe$_3$C, ε-Fe$_2$C, and FeO$_x$ species. The Fe$_x$C phase belongs to the iron phase with the Bhf value of 11.05 T (Table S3). The K-Fe/NC-fresh-P exhibit strong fitting peaks of FeO$_x$, accounting for 38.6%. The ε-Fe$_2$C phase is in good accordance with the XRD results (Fig. 3F). The K-Fe/NC-spent-2 h-P catalyst demonstrates 51.1% of χ-Fe$_5$C$_2$, 19.7% of Fe$_3$O$_4$ and 29.2% of FeO$_x$, which means the various iron carbides/nitrides in the K-Fe/NC-fresh-P catalyst were transformed into χ-Fe$_5$C$_2$ during the FTS process (Fig. 4B, E, Table S3). For the K-Fe/NC-spent-60 h-P catalyst, the ratio of χ-Fe$_5$C$_2$(I),

χ-Fe$_5$C$_2$(II), and χ-Fe$_5$C$_2$(III) is fixed to 2:2:1 to simulate the experimental data better (Fig. 4C, F). The emergence of χ-Fe$_5$C$_2$ and ε-Fe$_2$C phases in the K-Fe/NC-spent-60 h-P catalyst is reasonable and has been observed in the spent iron-base catalysts in FTS [36,37]. Hence, it can be concluded that the K-Fe/NC-spent-60 h-P catalyst mainly consists of χ-Fe$_5$C$_2$, ε-Fe$_2$C, and Fe$_3$O$_4$ phases as well as FeO$_x$ phase. Furthermore, the close contact between potassium and iron carbides enhances the crystallinity and stability of carbides.

The Mössbauer spectra of FeO$_x$ represent the doublet peak which means its superparamagnetic property and the small particle size (< 10 nm). The FeO$_x$ phase belongs to the shell of the K-Fe/NC particles. A surface oxide layer formed after passivation is usually amorphous, however, it could be transformed to crystalline magnetite (Fe$_3$O$_4$) under electron beam irradiation during TEM analysis [7,8,38,39]. The shell of amorphous FeO$_x$ is formed by air passivation, which is transformed into Fe$_3$O$_4$ phase by beam-induced heating during TEM analysis. Hence, the shell presents Fe$_3$O$_4$ phase in HRTEM (Figs. 2F, 3C). A small amount of Fe$_3$O$_4$ phases are generated during FTS in the spent K-Fe/NC catalyst, detected by Mössbauer spectra and XRD results, presenting in the bulk or the core of the iron particles. These Fe$_3$O$_4$ phases are hard to be observed from HRTEM due to their small amount and the beam-induced iron phase evolution, and only χ-Fe$_5$C$_2$ and ε-Fe$_2$C phases are observed in the core of the spent K-Fe/NC catalyst.

The characterization by TEM, XRD, and Mössbauer spectra can only determine the presence of iron phases and their amounts. However, the amount of accessible active sites is still unknown. The exposed active sites could be detected by the CO-TPD and the CO-TPSR. There are CO and CO$_2$ desorption peaks, accompanied by a small CH$_4$ desorption peak, for the TPD curves of K-Fe/NC-fresh-P catalyst without pretreatment (Fig. 5A). It is supposed that the desorbed CO comes from the oxidation of iron carbides by iron oxides. The desorbed CO$_2$ and CH$_4$ are generated from the interaction of the residual C, O and H elements in the K-Fe/NC-fresh-P catalyst during the TPD. The hydrogen pretreated K-Fe/NC-fresh-P catalyst presents a similar CO desorption peak area before and after pretreatment (Figs. S6A, S7, Table S4). The FeC$_x$/FeN$_x$ @FeO$_x$ core-shell particles in the K-Fe/NC-fresh-P catalyst were reduced to
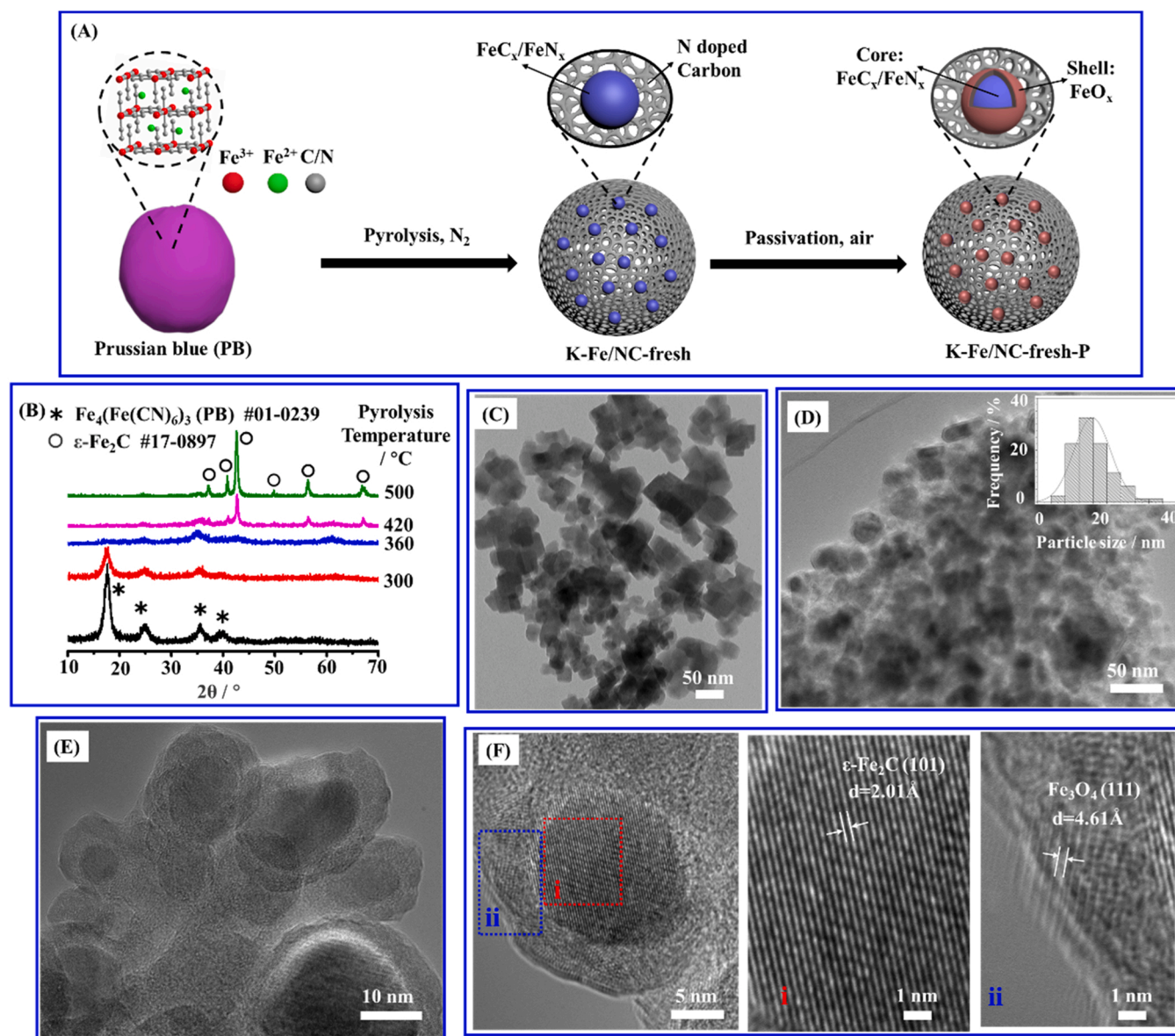
Fig. 2. Architectures of the fresh K-Fe/NC catalyst. Schematic diagram (A) and in situ XRD patterns (B) of the pyrolysis process from PB to the K-Fe/NC-fresh-P catalyst. The TEM image of PB (C) and the K-Fe/NC-fresh-P catalyst (D) with the size distribution histogram of the iron nanoparticles (the size distribution of iron nanoparticle size is obtained from TEM images analysis by using at least 100 nanoparticles), the overall HRTEM image (E), the HRTEM image and the corresponding lattice fringes (F) of the K-Fe/NC-fresh-P catalyst. K-Fe/NC-fresh denotes the freshly prepared K-Fe/NC catalyst without passivation. K-Fe/NC-fresh-P denotes the freshly prepared K-Fe/NC catalyst with air passivation.

metal iron (Fe^0) particles during the hydrogen pretreatment. The similar CO desorption peak area of the sample without pretreatment and with hydrogen pretreatment implies that the metal iron (Fe^0) phase does not adsorb CO. The syngas pretreated K-Fe/NC-fresh-P catalyst also presents a similar CO desorption peak area to that without pretreatment (Figs. S6B, S7, Table S4). It is supposed that the FeO_x shell of the FeC_x/ FeN_x @FeO_x particles in the K-Fe/NC-fresh-P catalyst can not be carbonized by syngas. The similar CO desorption peak area of the sample without and with syngas pretreatment implies the air passivated FeO_x shell does not absorb CO, indicating the FeO_x shell can not be carbonized by the syngas pretreatment. The tiny difference in the desorption temperature and peak area for K-Fe/NC-fresh-P catalyst without or with hydrogen/syngas pretreatment might be related to the slight change of iron state induced by various pretreatments (Fig. S7, Table S4).

The K-Fe/NC-fresh-P catalysts pretreated by CO for 0.3 h and 2 h manifest considerable CO and CO_2 desorption peaks even in comparison with that of the sample without pretreatment (Fig. 5B, C). Generally, the

first CO desorption peak corresponds to the weakly adsorbed CO and the second peak to the strongly adsorbed CO [40]. The strongly adsorbed CO may induce the dissociation of CO into C* and O* and the weakly adsorbed CO may produce the associated CO* during FTS reaction [41]. The CO_2 desorption peaks come from the reaction between the weakly adsorbed CO and the O element of the sample itself. The CH_4 desorption peaks are generated from the interaction between the trace dissociated C* and the residual hydrogen of the sample itself [42]. The CO pretreatment is generally known as an effective approach to transform iron oxides into iron carbides [37,43]. We may suppose the χ–Fe_5C_2, ε–Fe_2C and Fe_3O_4 phases of the K-Fe/NC catalyst are the main accessible active phases for CO adsorption. The CO-0.3 h pretreated K-Fe/NC-fresh-P catalyst presents two significant CO desorption peaks at 489.6 °C and 628.3 °C and the corresponding peak areas of 7.2 and 16.9, respectively (Fig. 5D). The CO desorption peak temperatures and area of the CO-2 h pretreated sample are both lower than that of the CO-0.3 h pretreated sample, indicating the increase of CO pretreatment time may decrease
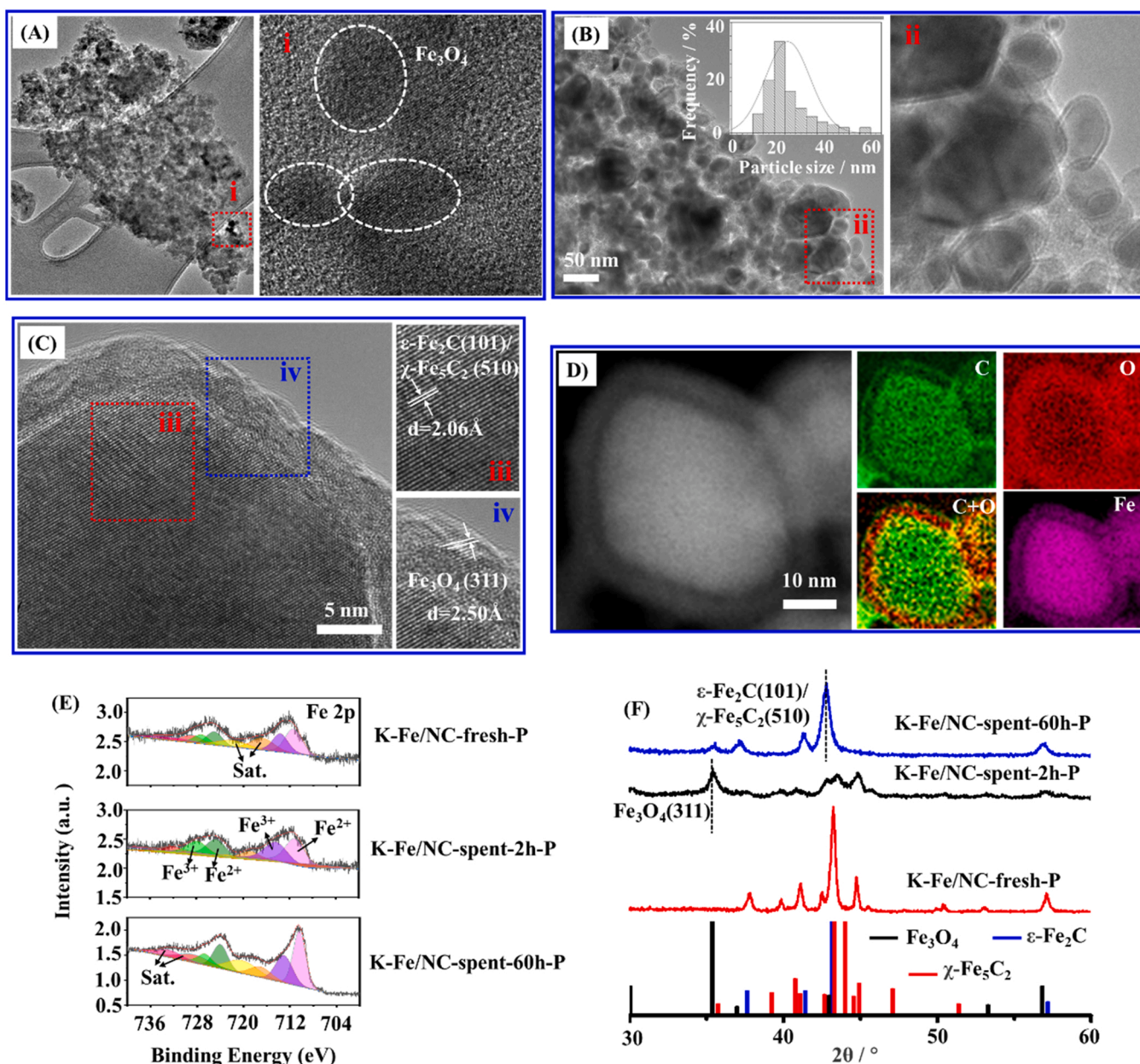
Fig. 3. TEM image of 15Fe/SiO$_2$ (A). The overall TEM image (B) with the size distribution histogram of the iron nanoparticles (the size distribution of iron nanoparticle size is obtained from TEM images analysis by using at least 100 nanoparticles), HRTEM image and the corresponding lattice fringes (C), the STEM and EDS elemental mapping images (D) of the K-Fe/NC-spent-60 h-P catalyst. XPS spectra of Fe 2p (E) and XRD patterns (F) and of the K-Fe/NC catalysts. K-Fe/NC-spent-2 h-P and K-Fe/NC-spent-60 h-P denote the spent K-Fe/NC catalysts with TOS of 2 h and 60 h as well as the air passivation, respectively.

the CO adsorption amount and reduce the CO adsorption active sites. The peak area and temperatures of CO, CH$_4$, and CO$_2$ exhibit the same trend (Fig. S7, Table S4). The increase in the CO pretreatment time may lead to more carbon deposition on the exposed active sites, resulting in less accessible active sites for CO adsorption [12–14,37].

CO-TPSR experiments are designed to further confirm the accessible active sites for CO dissociation and association. As shown in Fig. 5E, the CO-TPSR spectra of the CO pretreated K-Fe/NC-fresh-P catalyst mainly exhibits the desorption peaks of CO, CO$_2$, CH$_4$, OH* and H$_2$O. The localization and the area of the peak can provide information about the amount of accessible active sites for CH$_4$ formation (Figs. S8, S9, Table S5). During the CO adsorption (10% CO/He) step, the strongly adsorbed CO undergoes the H-assisted CO dissociation on the χ–Fe$_5$C$_2$/ ε-Fe$_2$C active sites, forming C* and O* (Fig. S10). Simultaneously, the weakly adsorbed CO experiences CO association on the Fe$_3$O$_4$ active site,

forming CO* . When the hydrogen (10% H$_2$/He) is introduced to the CO-TPSR system in the subsequent step, the formed C* may react with H* to form CH$_4$, while the dissociated O* may react with H* to form OH* . The similar position and shape of CH$_4$ and OH* peaks confirm their formation mechanism (Fig. 5E). The dissociated CO plays an important role in chain growth. The associated CO may insert into the chain growth, forming alcohol. The amount of dissociated and associated CO is essential for tuning the alcohol selectivity.

The CO$_2$ peak generates from the reaction between the associated CO* and the O element from the sample itself. The O element of the sample itself may react with H* to form H$_2$O. The O and C elements of the sample itself may interact with each other, forming CO. According to the literature [44,45], CH$_4$ is difficult to be adsorbed and it may be desorbed immediately once generated. Thus, the temperature of CH$_4$ desorption peak corresponds to the temperature of methane generation.
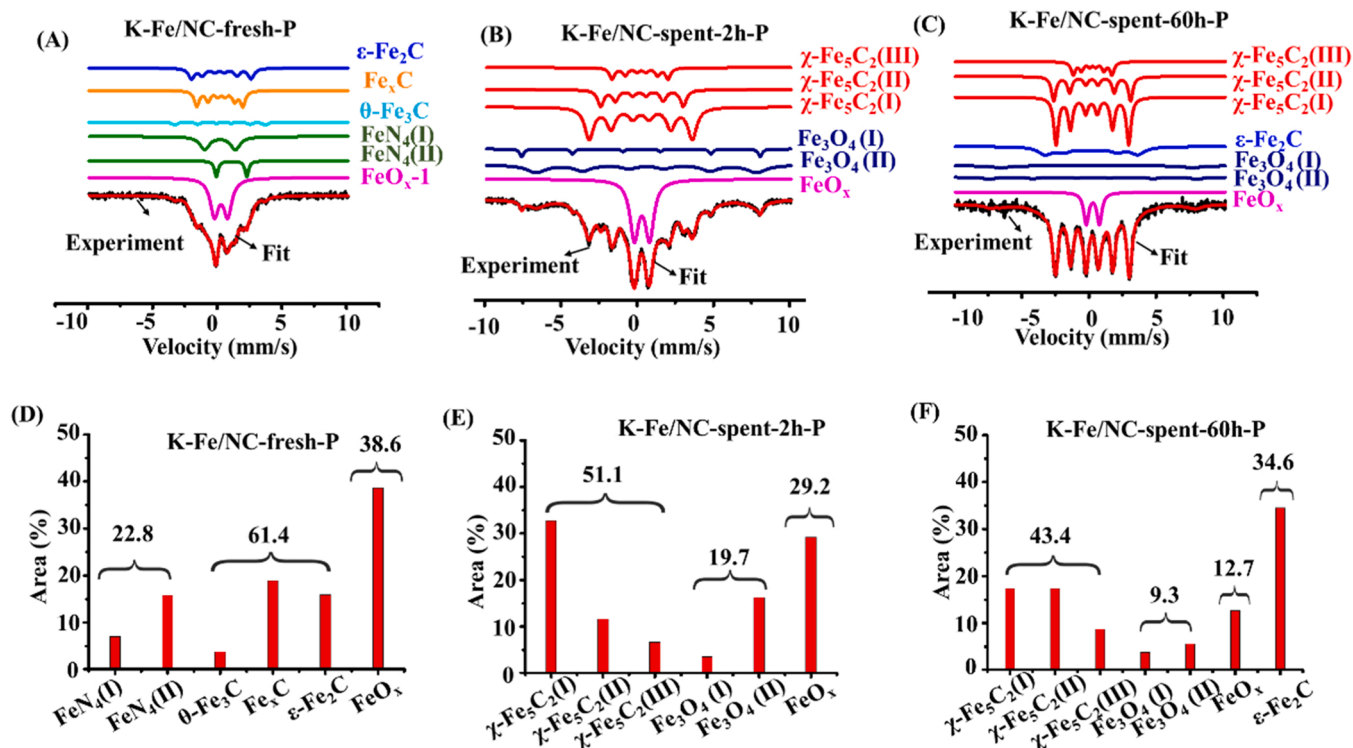
Fig. 4. The Mössbauer spectra for the K-Fe/NC-fresh-P (A), the K-Fe/NC-spent-2 h-P (B), and the K-Fe/NC-spent-60 h-P catalyst (C). The content of various iron phases obtained from the Mössbauer spectra of the K-Fe/NC-fresh-P (D), the K-Fe/NC-spent-2 h-P (E), and the K-Fe/NC-spent-60 h-P catalyst (F).
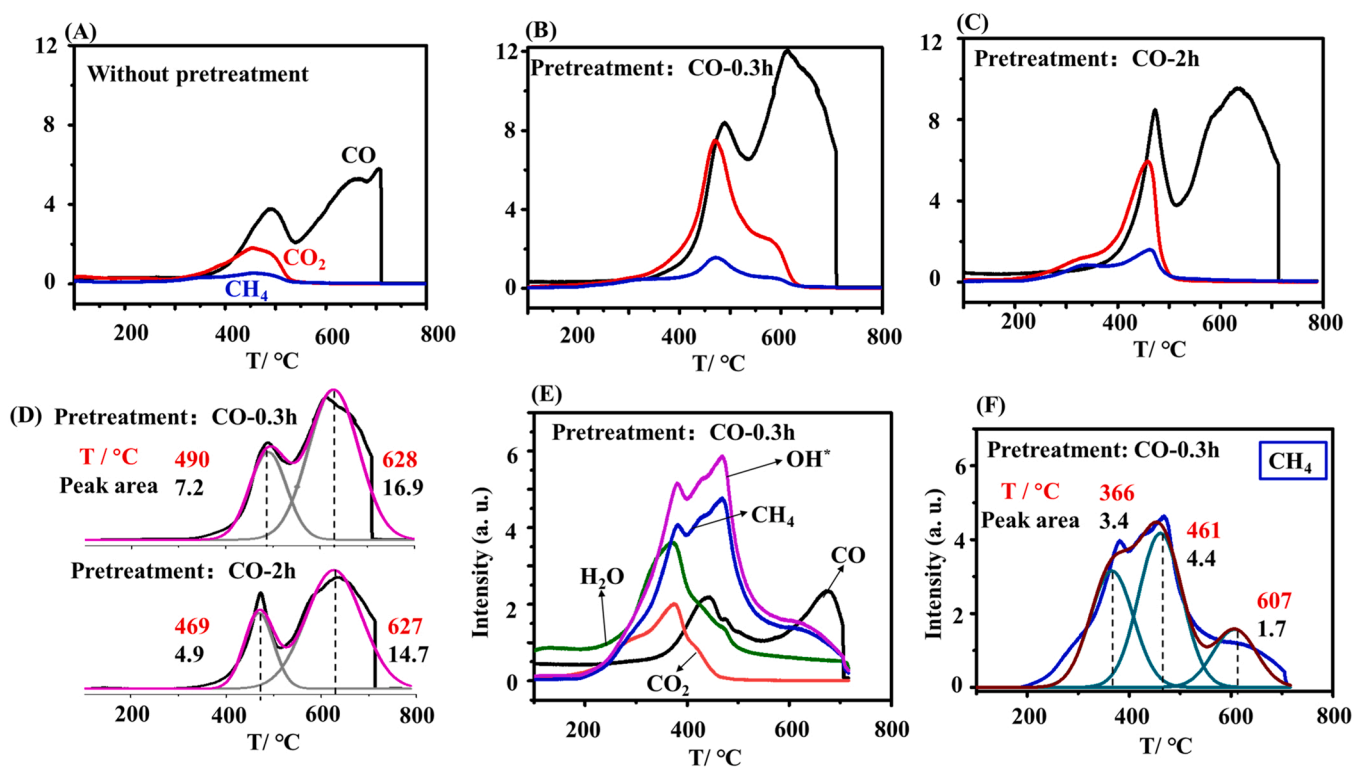

Fig. 5. CO-TPD and CO-TPSR results. The TPD profiles of the K-Fe/NC-fresh-P catalyst without pretreatment (A), with CO pretreatment at 240 °C for 0.3 h (B) and 2 h (C). The peak area of CO from the TPD files (D). The CO-TPSR profiles of the K-Fe/NC-fresh-P catalyst with CO pretreatment at 240 °C for 0.3 h (E). The peak area of CH_4 from the CO-TPSR profiles with CO pretreatment for 0.3 h (F). CO: black line. CO_2: red line. CH_4: blue line. OH* : pink line. H_2O: green line.

The lower the temperature of CH_4 desorption peak, the easier the CO dissociation on the χ–Fe_5C_2 active sites. Meanwhile, the CH_4 desorption peak area corresponds to the amount of the dissociated CO, which is further correlated to the amount of the accessible χ–Fe_5C_2/ε-Fe_2C active sites. Similarly, the desorption peak area of CO_2 should correspond to the amount of accessible Fe_3O_4 sites (Table S5). The desorption temperatures of CH_4 exhibit an increasing trend with the increase of the pretreatment time, indicating that the CO dissociation becomes more difficult (Fig. 5F). This result may be related to higher carbon deposition induced by the increase of the pretreatment time, which is consistent with the CO-TPD results.

3.3. Structure-performance relationship

The CO conversion presents a downward trend at the initial stage of the reaction (Fig. 1A). There are many reasons for the decrease of activity, such as agglomeration of Fe nanoparticles, and carbon deposition [46]. The particle size distribution of the K-Fe/NC-fresh-P and K-Fe/NC-spent-60 h-P demonstrates that there is nearly no aggregation of metal particles during the reaction (Figs. 2D, 3B). CO-TPD and CO-TPSR results have confirmed that the longer CO pretreatment time may cause more severe carbon deposition (Fig. 5). The XPS confirms that the surface content of carbon increased from 17.4% of K-Fe/NC-fresh-P to 67.6% of K-Fe/NC-spent-60 h-P (Fig. S5). TG analysis shows 14.7% weight loss in the spent K-Fe/NC catalyst due to the carbon deposition (Fig. S11). The K element in K-Fe/NC catalyst also promotes carbon deposition. Moreover, the chain length of the paraffins in the oil product for the initial reaction stage is longer than that for the stable reaction stage (Fig. 1B, E) at a similar chain growth factor of about 0.61 for alcohols (Fig. 1C, F). It is supposed that the paraffin product is mainly produced on the χ–Fe_5C_2 / ε-Fe_2C active sites and the alcohol product on the χ–Fe_5C_2 / ε-Fe_2C and Fe_3O_4 dual active sites. The χ–Fe_5C_2 / ε-Fe_2C active sites are reducing as the reaction processes due to the carbon deposition, leading to the decreased CO conversion at the initial stage and less long chain length of paraffins in the stable stage (Fig. 1A, E). The relatively small amount of Fe_3O_4 active sites makes the alcohol chain length less affected by the decrease of the χ–Fe_5C_2 / ε-Fe_2C active sites.

The presence of nitrogen has been reported as an important factor affecting the catalytic performance of Fe-based catalysts. There is a certain amount of nitrogen in the K-Fe/NC catalyst. Fe@NC with N-doped carbon shell demonstrates higher activity and approximative selectivity compared to Fe@C with a pure carbon shell (Table S6) [47]. For the application of MOF derived Co@NC in FTS, it is assumed no correlation between the catalytic performances and the amount of nitrogen in the carbon matrix, which exists as pyridinic or graphitic nitrogen species [48]. The Fe/N-CNT catalysts with N doping demonstrate superior FTS activity than Fe/CNT catalysts with N doping [49]. The pyrrolic N in the N-doped carbon nanosheets facilitated iron carbonization and enhanced the activity [50]. According to the literature, the main contribution of N doping in FTS is related to its enhanced activity and olefin selectivity. The enhanced activity is generally derived from the facilitated iron carbonization induced by the N element. The enhanced olefin selectivity results from the N element serving as an electron donor to weaken the adsorption of hydrogen. It is supposed the N doped carbon matrix of the K-Fe/NC catalyst may enhance the activity and olefin selectivity to some extent.

Another element, which could affect the catalytic performance of K-Fe/NC catalyst is potassium. The K element is generally considered a strong electron donor to weaken the adsorption capability of the H_2 and enhance the olefin selectivity in FTS [10,51,52]. The potassium-promoted iron catalyst demonstrates lower methane selectivity, higher C_5 + selectivity and higher olefins/paraffins ratio than the pure iron catalyst (Table 1). The addition of potassium increases the amount of iron carbides formed in FTS, which further influences the catalytic performance [53,54]. Herein, the alcohol selectivity of K-Fe/NC catalyst is more relevant to the CO dissociation and association

that occurred in various iron phases. It is supposed that potassium plays a positive role in the formation of iron carbides. The relationship between the formed carbides and alcohol formation is emphasized for the K-Fe/NC catalyst. For the LTFTS process of the impregnated 15Fe/SiO_2 catalyst, the WGS reaction is relatively slow due to the kinetically unfavorable properties of WGS at low temperatures (Table 1) [31,55]. The addition of manganese and potassium can enhance the WGS reaction [30]. The WGS reaction can adjust the hydrogen content in syngas, especially benefitting the coal-based syngas with a low H/C ratio (H_2/CO = 0.5–0.7). The high rate of WGS reaction results in a hydrogen-rich environment which attributes to the short chain length of the oil product. Meanwhile, the high selectivity for long-chain alcohols with high contribution of C_2 + alcohols (95%) is another feature of the K-Fe/NC catalyst. The high selectivity for C_2 + alcohols could be assigned to the joint effect of N doped carbon and K promoter. As mentioned above, the K promoter can enhance the chain growth and prohibit the hydrogenation reaction. Hence, there are more long-chain hydrocarbon intermediates in the reaction atmosphere, the associated CO tends to insert into the long-chain hydrocarbon to form long-chain alcohols. Similarly, the small amount of N element in the K-Fe/NC may also play a positive role in the formation of long-chain alcohols. The preparation of the catalyst using PB precursor provides an opportunity to incorporate N and K in the close proximity to Fe, which should significantly increase the electron density over Fe catalyst and suppress deep hydrogenation to paraffins providing an opportunity to increase selectivity to long chain alcohols.

3.4. DFT calculations

Theoretical calculations are performed to investigate the mechanism of CO dissociation on the Fe_3O_4(311), ε-Fe_2C(101) and χ-Fe_5C_2(510) surfaces. Firstly, the behavior of CO adsorption has been investigated. The most stable configurations and the adsorption free energies of the intermediates involved in the direct or H-assisted CO dissociation are presented in Fig. S12 and Tables S7, S8. On Fe_3O_4(311), the most stable site of CO adsorption is Fe_{oct} at the step edges, the C-O bond length is elongated to 1.147 Å and the adsorption free energy is − 43.9 kJ mol^{-1}. On ε-Fe_2C (101), CO prefers to adsorb at the Fe top site with the C-O bond length of 1.165 Å and the adsorption free energy of − 67.3 kJ mol^{-1}. On χ-Fe_5C_2(510), CO is bounded to 3 F site via C atom with the adsorption free energy of − 115.1 kJ mol^{-1} and the C-O bond length is elongated to 1.202 Å. Thus, the stronger CO adsorption energy can elongate the C-O bond length of CO, which follows the order: Fe_3O_4(311) < ε-Fe_2C(101) < χ-Fe_5C_2(510). The free energy profile of CO dissociation on the three surfaces and the optimized configurations of initial states, transition states and final states are presented. The direct CO dissociation on Fe_3O_4(311) is hindered by the high activation free energy of 594.0 kJ mol^{-1}, it is endothermic by 383.1 kJ mol^{-1} (Figs. 6A, D, S13). The overall activation free energy and reaction free energy of H-assisted CO dissociation is 429.6 and 209.5 kJ mol^{-1}. The direct CO dissociation and H-assisted CO dissociation have the highest activation free energy, namely, CO dissociation is very difficult to occur on Fe_3O_4(311) surface.

On ε-Fe_2C(101), H-assisted CO dissociation via CHO* intermediate has the overall activation free energy of 195.5 kJ mol^{-1} and the reaction free energy of 28.2 kJ mol^{-1}, which are very close to the direct CO dissociation (195.2 and 9.3 kJ mol^{-1}) (Fig. 6B, E). Thus, CO dissociation is carried out by both the direct and H-assisted CO dissociation mechanisms. On χ-Fe_5C_2(510), CO direct dissociation is more favorable in kinetics and thermodynamics compared to the H-assisted CO dissociation route (110.8 and −70.7 vs. 133.4 and −59.5 kJ mol^{-1}) (Fig. 6C, F). Based on the above analysis, CO association adsorption dominantly occurs on Fe_3O_4(311) surface instead of CO dissociation. Both direct CO dissociation and H-assisted CO dissociation are likely to occur on the ε-Fe_2C(101). Interestingly, χ-Fe_5C_2(510) surface is more active for direct CO dissociation.
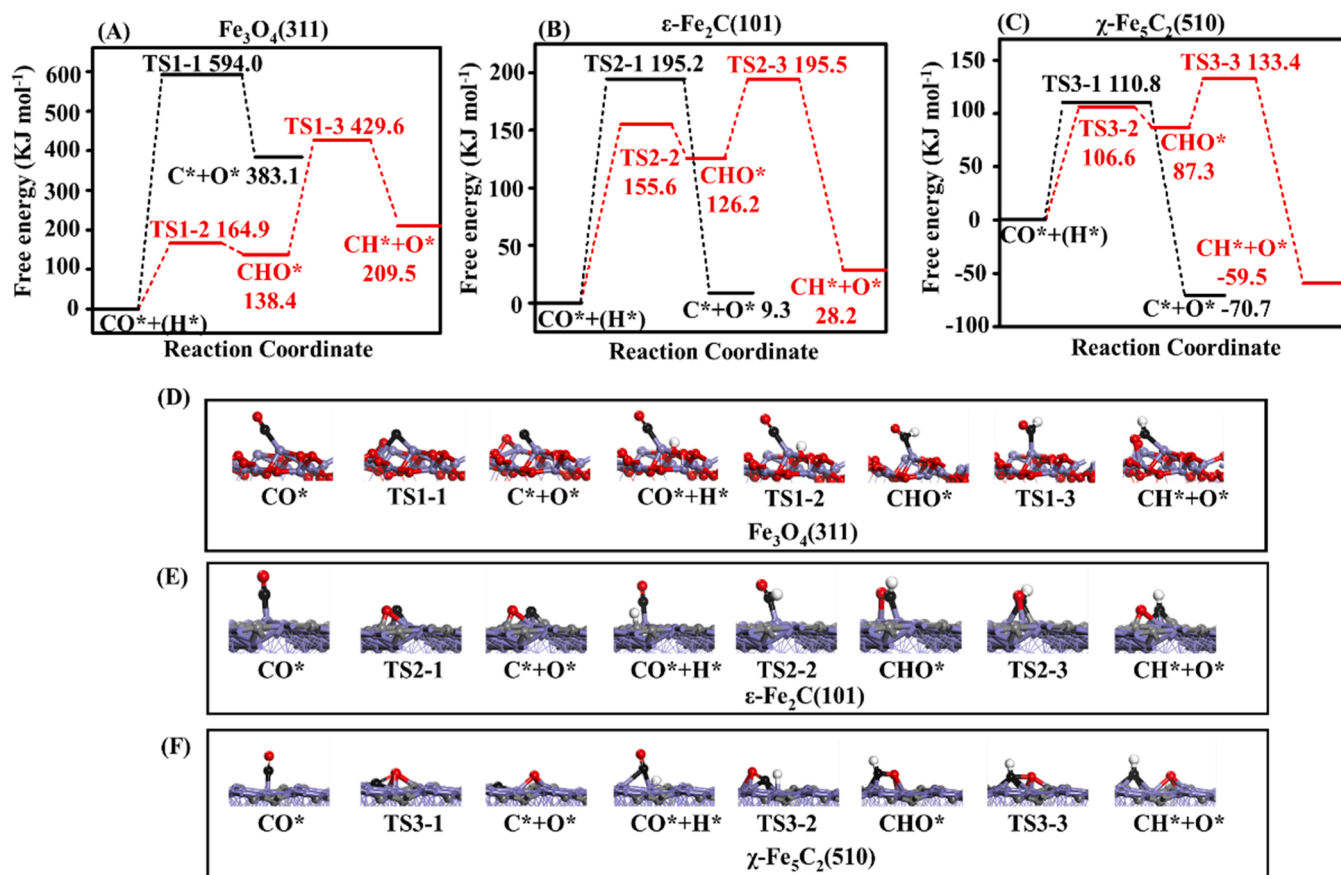
Fig. 6. Free energy profiles of the direct and H-assisted CO dissociation on the Fe_3O_4(311) (A), ε-Fe_2C(101) (B) and χ-Fe_5C$_2$(510) surfaces (C). Black line: the direct CO dissociation; Red line: H-assisted CO dissociation via CHO* intermediate. Structures of the initial states, transitional states and final states involving in the direct or H-assisted CO dissociation on the Fe_3O_4(311) (D), ε-Fe_2C(101) (E) and χ-Fe_5C$_2$(510) (F) surfaces. Purple: Fe atom, red: O atom, gray: C atom, black: C atom in molecules, white: H atom.

3.5. The alcohol formation mechanism

The schematic diagram of the structure and phase evolution of K-Fe/NC catalyst is shown in Fig. 7A. The K-Fe/NC-fresh catalyst is obtained through PB in situ pyrolysis, which is mainly composed of Fe_xC/FeN_x phases with particle sizes around 20 nm. Hence, the spent K-Fe/NC catalysts undergo the structure and phase evolution during FTS and the subsequent air passivation. The final sample demonstrates an A@B core-shell structure with the χ–Fe_5C$_2$/ε-Fe_2C/Fe_3O_4 particles as the core of A and the FeO_x as the shell of B. The core-shell structure of the spent iron particles in FTS has been noticed in the literature [12–15], yet it is still controversial about the exact structure of the spent iron catalysts. Herein, we confirmed the formation process of the core-shell structure during FTS and the passivation process. CO dissociation over χ–Fe_5C$_2$ phase has been widely considered as the main reason for the chain growth of hydrocarbons [42,56,57]. The CO insertion mechanism has usually been known as the reason for alcohol formation in FTS [58–60]. The synergetic effect of dual active sites has been recognized as an alcohol formation mechanism in FTS over the activated carbon supported cobalt (Co/AC) catalyst. The Co_2C and metal Co species are responsible for CO association and dissociation, respectively, which serve as the dual active sites for alcohol formation [61,62]. However, only a few publications are showing the active sites for alcohol products over iron-based catalysts.

Fe_3O_4 has been considered to be the active site for reverse water gas shift reaction (RWGS) in CO_2 hydrogenation [63,64]. Fe_3O_4 is also active for WGS reaction and high CO_2 selectivity has been observed for this K-Fe/NC catalyst (Table 1). DFT calculation confirms the CO

association on Fe_3O_4 and CO dissociation on χ–Fe_5C$_2$ and ε-Fe_2C phases. Hence, the alcohol formation mechanism of the K-Fe/NC catalyst is proposed (Fig. 7B). CO dissociation occurs on the χ–Fe_5C$_2$/ε-Fe_2C active sites forming C* and O* , and CO association occurs on the Fe_3O_4 active sites forming CO* . The alcohols are produced on the interface of χ–Fe_5C$_2$/ε-Fe_2C and Fe_3O_4 through the CO* insertion into the chain growth. Simultaneously, the formed CO* also reacts with OH* to generate CO_2 and H_2, resulting in a hydrogen-rich reaction environment. Hence, the synergistic effect of the χ–Fe_5C$_2$/ε-Fe_2C and Fe_3O_4 dual active sites benefits alcohol formation. Due to the high alcohol selectivity for K-Fe/NC catalyst, it is considered that the proportion of χ–Fe_5C$_2$/ε-Fe_2C and Fe_3O_4 accessible active sites seem to be responsible for high alcohol selectivity in FTS. It might be further endeavors for promoting alcohol selectivity through increasing the amount of Fe_3O_4 accessible active sites close to Fe carbide to induce more insertion of associated CO into the chain growth.

4. Conclusion

The K-Fe/NC catalyst has been designed and fabricated through PB pyrolysis, displaying low-cost and scalable-produced features. The in situ activated K-Fe/NC catalyst demonstrated alcohol selectivity as high as 30% in FTS, with the alcohol distribution of 5% methanol, 56% C_2-C_5 alcohols, and 39% C_6-C_{13} alcohols. The iron time yield of the K-Fe/NC catalysts is 11 mmol$_{CO}$ g$_{Fe}^{-1}$ h^{-1}. The K-Fe/NC catalyst undergoes the structure and phase evolution during FTS and the subsequent air passivation, demonstrating an A@B core-shell structure with the χ–Fe_5C$_2$/ε-Fe_2C/Fe_3O_4 particles as the core of A and the FeO_x as the shell
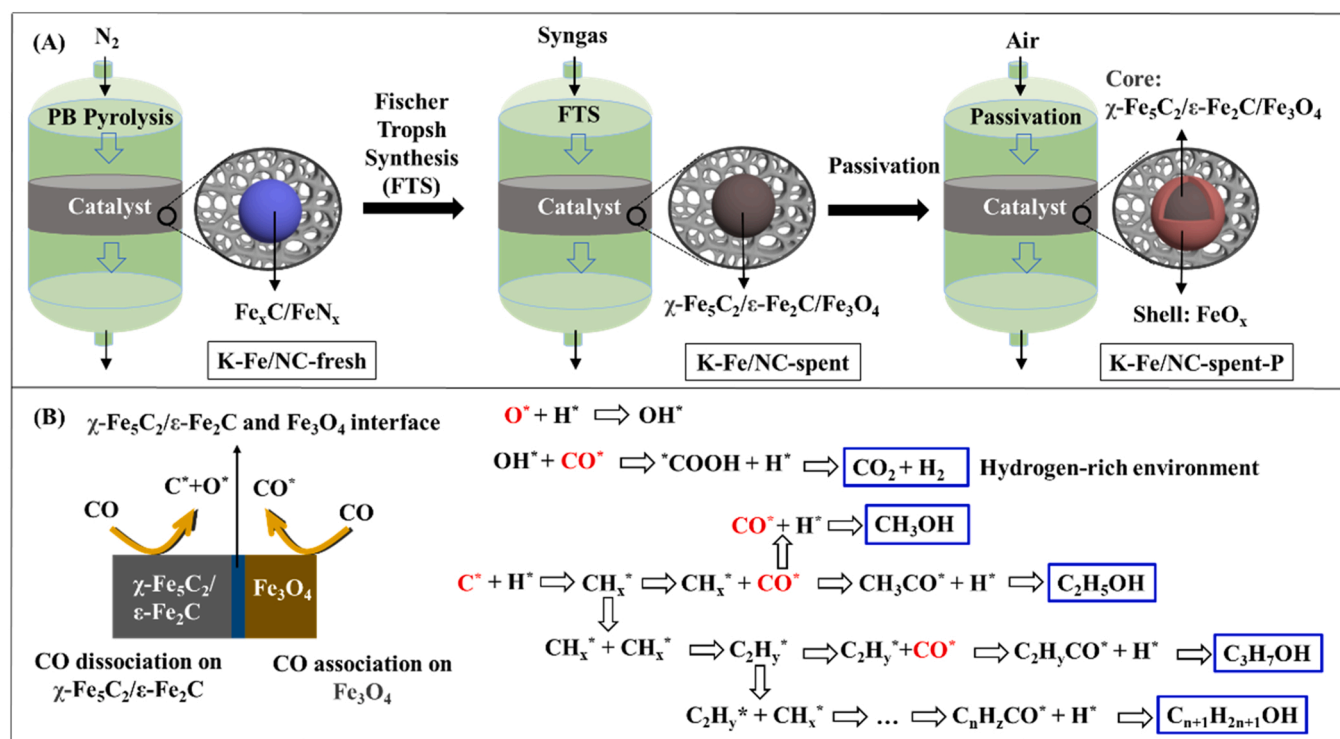
Fig. 7. Schematic diagram of the structure and phase evolution of the K-Fe/NC catalyst during FTS reaction and the air passivation process (A). The active sites and the corresponding alcohol formation mechanism on the K-Fe/NC catalyst (B).

of B. The TPD/TPSR results and theoretical calculations confirmed CO underwent CO dissociation on the χ–Fe_5C_2/ε-Fe_2C active sites and experienced CO association on the Fe_3O_4 active sites. The alcohol formation was benefited from the synergistic effect of χ–Fe_5C_2/ε-Fe_2C and Fe_3O_4 dual active sites, and the alcohol was formed through the insertion of the associated CO into the chain growth. This work is of fundamental importance in the understanding of the alcohol formation mechanism in FTS. Furthermore, it provides significant insight into the development of low-cost and highly efficient iron-based catalysts for alcohols in FTS.

CRediT authorship contribution statement

Y.P. Chen conceived the idea for the project and wrote the manuscript. L.X. Ma and R.G. Zhang performed the DFT calculation. J.T. Wei performed the catalytic preparation and catalytic test experiments. R.P. Ye performed the catalyst characterization. V.V. Ordomsky and J. Liu conceived the idea for the project and supervised the project.

Declaration of Competing Interest

The authors declare that they have no known competing financial interests or personal relationships that could have appeared to influence the work reported in this paper.

Appendix A. Supporting information

Supplementary data associated with this article can be found in the online version at doi:10.1016/j.apcatb.2022.121393.

References

[1] A.Y. Khodakov, W. Chu, P. Fongarland, Advances in the development of novel cobalt Fischer–Tropsch catalysts for synthesis of long-chain hydrocarbons and clean fuels, Chem. Rev. 107 (2007) 1692–1744.
[2] Y. Chen, J. Wei, M.S. Duyar, V. Ordomsky, J. Liu, Carbon-based catalysts for Fischer–Tropsch synthesis, Chem. Soc. Rev. 50 (2021) 2337–2366.
[3] M. Ao, G.H. Pham, J. Sunarso, M.O. Tade, S. Liu, Active centers of catalysts for higher alcohol synthesis from syngas: a review, ACS Catal. 8 (2018) 7025–7050.
[4] H.M. Torres Galvis, J.H. Bitter, C.B. Khare, M. Ruitenbeek, A.I. Dugulan, K.P. de Jong, Supported iron nanoparticles as catalysts for sustainable production of lower olefins, Science 335 (2012) 835–838.
[5] V.V. Ordomsky, Y. Luo, B. Gu, A. Carvalho, P.A. Chernavskii, K. Cheng, A. Y. Khodakov, Soldering of iron catalysts for direct synthesis of light olefins from syngas under mild reaction conditions, ACS Catal. 7 (2017) 6445–6452.
[6] Y. Chen, Y. Ni, Y. Liu, H. Liu, X. Ma, S. Liu, W. Zhu, Z. Liu, Sintered precipitated iron catalysts with enhanced fragmentation-resistance ability for Fischer–Tropsch synthesis to lower olefins, Catal. Sci. Technol. 8 (2018) 5943–5954.
[7] Y. Jin, A.K. Datye, Phase transformations in iron Fischer–Tropsch catalysts during temperature-programmed reduction, J. Catal. 196 (2000) 8–17.
[8] L.D. Mansker, Y. Jin, D.B. Bukur, A.K. Datye, Characterization of slurry phase iron catalysts for Fischer–Tropsch synthesis, Appl. Catal. A 186 (1999) 277–296.
[9] M. Qing, Y. Yang, B. Wu, J. Xu, C. Zhang, P. Gao, Y. Li, Modification of Fe–SiO2 interaction with zirconia for iron-based Fischer–Tropsch catalysts, J. Catal. 279 (2011) 111–122.
[10] V.V. Ordomsky, A. Carvalho, B. Legrasa, S. Paul, M. Virginie, V.L. Sushkevich, A. Y. Khodakov, Effects of co-feeding with nitrogen-containing compounds on the performance of supported cobalt and iron catalysts in Fischer-Tropsch synthesis, Catal. Today 275 (2016) 84–93.
[11] M.I. Fadlalla, S.G. Babu, T.M. Nyathi, K.J. Weststrate, M. Claeys, Enhanced oxygenates formation in the Fischer–Tropsch synthesis over Co- and/or Ni-containing Fe alloys: characterization and 2D gas chromatographic product analysis, ACS Catal. 10 (2020) 14661–14677.
[12] M.D. Shroff, D.S. Kalakkad, K.E. Coulter, S.D. Kohler, M.S. Harrington, N. B. Jackson, A.G. Sault, A.K. Datye, Activation of precipitated iron Fischer-Tropsch synthesis catalysts, J. Catal. 156 (1995) 185–207.
[13] M. Ding, Y. Yong, B. Wu, T. Wang, L. Ma, H. Xiang, Y. Li, Transformation of carbonaceous species and its influence on catalytic performance for iron-based Fischer–Tropsch synthesis catalyst, J. Mol. Catal. A 351 (2011) 165–173.

[14] M. Ding, Y. Yang, B. Wu, Y. Li, T. Wang, L. Ma, Study on reduction and carburization behaviors of iron phases for iron-based Fischer–Tropsch synthesis catalyst, Appl. Energy 160 (2015) 982–989.

[15] B.H. Davis, Fischer-Tropsch Synthesis, Catalysts, and Catalysis, Vol. 163 (B.H. Davis, M.L. Occelli), Elsevier, 2007, Ch. 3.

[16] Y. Lu, B. Cao, F. Yu, J. Liu, Z. Bao, J. Gao, High selectivity higher alcohols synthesis from syngas over three-dimensionally ordered macroporous Cu-Fe catalysts, ChemCatChem 6 (2014) 473–478.

[17] M.A. Haider, M.R. Gogate, R.J. Davis, Fe-promotion of supported Rh catalysts for direct conversion of syngas to ethanol, J. Catal. 261 (2009) 9–16.

[18] H. Du, H. Zhu, Z. Zhao, W. Dong, W. Luo, W. Lu, M. Jiang, T. Liu, Y. Ding, Effects of impregnation strategy on structure and performance of bimetallic CoFe/AC catalysts for higher alcohols synthesis from syngas, Appl. Catal. A 523 (2016) 263–271.

[19] X. Zhang, Z. Li, Q. Guo, H. Zheng, K. Xie, Selective synthesis of mixed alcohols from syngas over catalyst Fe_2O_3/Al_2O_3 in slurry reactor, Fuel Process. Technol. 91 (2010) 379–382.

[20] Y. Lian, H. Sun, X. Wang, P. Qi, Q. Mu, Y. Chen, J. Ye, X. Zhao, Z. Deng, Y. Peng, Carved nanoframes of cobalt-iron bimetal phosphide as a bifunctional electrocatalyst for efficient overall water splitting, Chem. Sci. 10 (2019) 464–474.

[21] M. Zhang, M. Wang, B. Xu, D. Ma, How to measure the reaction performance of heterogeneous catalytic reactions reliably, Joule 3 (2019) 2876–2883.

[22] G. Kresse, J. Furthmüller, Efficiency of ab-initio total energy calculations for metals and semiconductors using a plane-wave basis set, Comput. Mater. Sci. 6 (1996) 15–50.

[23] J.P. Perdew, K. Burke, M. Ernzerhof, Generalized gradient approximation made simple, Phys. Rev. Lett. 77 (1996) 3865–3868.

[24] X. Han, Y. Li, H. Gong, Y. Wang, J. Lv, Y. Wang, S. Huang, X. Ma, Effect of Mn-dopant on carburization of the Fe_3O_4 catalysts in Fischer-Tropsch synthesis, Chem. Eng. Sci. 11 (2021), 100106.

[25] L. Ren, J. Xu, S. Pan, H. Yu, T. Zhang, T. Shoji, N. Li, D. Zhang, D. Sun, DFT studies on the interaction of $Fe^{2+}/Fe_3O_4(111)$ and $OH^-/Fe_3O_4(111)$ during the adsorption process in the steam generators of nuclear power plants, Colloids Surf. A 617 (2021), 126393.

[26] G.H. Barton, B. Gale, The structure of a pseudo-hexagonal iron carbide, Acta Crystallogr. 17 (1964) 1460–1462.

[27] S. Zhao, X. Liu, C. Huo, Y. Li, J. Wang, H. Jiao, Determining surface structure and stability of ε-Fe_2C, χ-Fe_5C_2, θ-Fe_3C and Fe_4C phases under carburization environment from combined DFT and atomistic thermodynamic studies, Catal. Struct. React. 1 (2014) 44–60.

[28] J.J. Retief, Powder diffraction data and rietveld refinement of Hägg-carbide, χ-Fe_5C_2, Powder Diffr. 14 (1999) 130–132.

[29] Y. He, P. Zhao, J. Yin, W. Guo, W. Yang, Y. Li, C. Huo, X. Wen, CO direct versus H-assisted dissociation on hydrogen coadsorbed χ-$Fe5C2$ Fischer–Tropsch catalysts, J. Phys. Chem. C (2018) 20907–20917.

[30] M. Ding, Y. Yang, J. Xu, Z. Tao, H. Wang, H. Wang, H. Xiang, Y. Li, Effect of reduction pressure on precipitated potassium promoted iron–manganese catalyst for Fischer–Tropsch synthesis, Appl. Catal. A 345 (2008) 176–184.

[31] X. Cui, J. Xu, C. Zhang, Y. Yang, P. Gao, B. Wu, Y. Li, Effect of pretreatment on precipitated Fe–Mo Fischer–Tropsch catalysts: Morphology, carburization, and catalytic performance, J. Catal. 282 (2011) 35–46.

[32] H. Wan, B. Wu, C. Zhang, H. Xiang, Y. Li, Promotional effects of Cu and K on precipitated iron-based catalysts for Fischer–Tropsch synthesis, J. Mol. Catal. A 283 (2008) 33–42.

[33] M. Hu, A.A. Belik, M. Imura, K. Mibu, Y. Tsujimoto, Y. Yamauchi, Synthesis of superparamagnetic nanoporous iron oxide particles with hollow interiors by using Prussian blue coordination polymers, Chem. Mater. 24 (2012) 2698–2707.

[34] C. Shi, S. Ye, X. Wang, F. Meng, J. Liu, T. Yang, W. Zhang, J. Wei, N. Ta, G. Lu, M. Hu, J. Liu, Modular construction of Prussian blue analog and TiO_2 dual-compartment janus nanoreactor for efficient photocatalytic water splitting, Adv. Sci. 8 (2021), 2001987.

[35] J. Liu, L. Wang, F. Okejiri, J. Luo, J. Zhao, P. Zhang, M. Liu, S. Yang, Z. Zhang, W. Song, W. Zhu, J. Liu, Z. Zhao, G. Feng, C. Xu, S. Dai, Deep understanding of strong metal interface confinement: a journey of Pd/FeO_x catalysts, ACS Catal. 10 (2020) 8950–8959.

[36] F. Lu, X. Chen, Z. Lei, L. Wen, Y. Zhang, Revealing the activity of different iron carbides for Fischer-Tropsch synthesis, Appl. Catal. B 281 (2021) 119521.

[37] L. Tang, L. He, Y. Wang, B. Chen, W. Xu, X. Duan, A.-H. Lu, Selective fabrication of χ-Fe_5C_2 by interfering surface reactions as a highly efficient and stable Fischer-Tropsch synthesis catalyst, Appl. Catal. B 284 (2021), 119753.

[38] R. Walker, A.D. Steele, D.T.B. Morgan, Pyrophoric nature of iron sulfides, Ind. Eng. Chem. Res. 35 (1996) 1747–1752.

[39] M.D. Shroff, A.K. Datye, The importance of passivation in the study of iron Fischer-Tropsch catalysts, Catal. Lett. 37 (1996) 101–106.

[40] B.H. Sakakini, Temperature-programmed surface reaction (TPSR) of pre-adsorbed carbon CO and CO/H_2 synthesis over Ru-Cs/Al_2O_3 catalysts, Mol. Catal. 127 (1997) 203–209.

[41] W. Ma, W.D. Shafer, G. Jacobs, J. Yang, D.E. Sparks, H.H. Hamdeh, B.H. Davis, Fischer-Tropsch synthesis: effect of CO conversion on CH_4 and oxygenate selectivities over precipitated Fe-K catalysts, Appl. Catal. A 560 (2018) 144–152.

[42] G. Jiao, Y. Ding, H. Zhu, X. Li, J. Li, R. Lin, W. Dong, L. Gong, Y. Pei, Y. Lu, Effect of La_2O_3 doping on syntheses of C_1–C_{18} mixed linear α-alcohols from syngas over the Co/AC catalysts, Appl. Catal. A 364 (2009) 137–142.

[43] R. Yao, J. Wei, Q. Ge, J. Xu, Y. Han, Q. Ma, H. Xu, J. Sun, Monometallic iron catalysts with synergistic Na and S for higher alcohols synthesis via CO_2 hydrogenation, Appl. Catal. B 298 (2021), 120556.

[44] J.G. Mccarty, H. Wise, Hydrogenation of surface carbon on alumina-supported nickel, Am. Chem. Soc. Div. Pet. Chem. Prepr. 22 (1979) 406–416.

[45] M. Ojeda, M.L. Granados, S. Rojas, P. Terreros, F.J. Garcia-Garcia, J.L.G. Fierro, Manganese-promoted Rh/Al_2O_3 for C_2-oxygenates synthesis from syngas: effect of manganese loading, Appl. Catal. A 261 (2004) 47–55.

[46] E. de Smit, B.M. Weckhuysen, The renaissance of iron-based Fischer-Tropsch synthesis: on the multifaceted catalyst deactivation behaviour, Chem. Soc. Rev. 37 (2008) 2758–2781.

[47] B. An, K. Cheng, C. Wang, Y. Wang, W. Lin, Pyrolysis of metal–organic frameworks to $Fe_3O_4@Fe_5C_2$ core–shell nanoparticles for Fischer–Tropsch synthesis, ACS Catal. 6 (2016) 3610–3618.

[48] Q. Luo, L. Guo, S. Yao, J. Bao, Z. Liu, Z. Liu, Cobalt nanoparticles confined in carbon matrix for probing the size dependence in Fischer-Tropsch synthesis, J. Catal. 369 (2019) 143–156.

[49] H. Xiong, M.A. Motchelaho, M. Moyo, L.L. Jewell, N.J. Coville, Fischer–Tropsch synthesis: Iron-based catalysts supported on nitrogen-doped carbon nanotubes synthesized by post-doping, Appl. Catal. A (2014) 377–386.

[50] Q. Zhao, S. Huang, X. Han, J. Chen, J. Wang, A. Rykov, Y. Wang, M. Wang, J. Lv, X. Ma, Highly active and controllable MOF-derived carbon nanosheets supported iron catalysts for Fischer-Tropsch synthesis, Carbon 173 (2021) 364–375.

[51] L. Niu, X. Liu, X. Liu, X. Wen, Y. Yang, J. Xu, Y. Li, Tuning carburization behaviors of metallic iron catalysts with potassium promoter and CO/syngas/C_2H_4/C_2H_2 gases, J. Catal. 371 (2019) 333–345.

[52] P. Zhang, F. Han, J. Yan, X. Qiao, Q. Guan, W. Li, N-doped ordered mesoporous carbon (N-OMC) confined Fe_3O_4-FeC_x heterojunction for efficient conversion of CO_2 to light olefins, Appl. Catal. B 299 (2021), 120639.

[53] Y. Yang, Effect of potassium promoter on precipitated iron-manganese catalyst for Fischer-Tropsch synthesis, Appl. Catal. A 266 (2004) 181–194.

[54] X. An, B. Wu, H. Wan, T. Li, Z. Tao, H. Xiang, Y. Li, Comparative study of iron-based Fischer–Tropsch synthesis catalyst promoted with potassium or sodium, Catal. Commun. 8 (2007) 1957–1962.

[55] M. Qing, Y. Yang, B. Wu, J. Xu, C. Zhang, P. Gao, Y. Li, Modification of Fe–SiO_2 interaction with zirconia for iron-based Fischer–Tropsch catalysts, J. Catal. 279 (2011) 111–122.

[56] M. Zhu, I.E. Wachs, Iron-based catalysts for the high-temperature water–gas shift (HT-WGS) reaction: a review, ACS Catal. 6 (2015) 722–732.

[57] J. Wang, S. Huang, S. Howard, B.W. Muir, H. Wang, D.F. Kennedy, X. Ma, Elucidating surface and bulk phase transformation in Fischer–Tropsch synthesis catalysts and their influences on catalytic performance, ACS Catal. 9 (2019) 7976–7983.

[58] J.P. Hindermann, G.J. Hutchings, A. Kiennemann, Mechanistic aspects of the formation of hydrocarbons and alcohols from CO hydrogenation, Catal. Rev. 35 (1993) 1–127.

[59] B.H. Davis, Fischer–Tropsch synthesis current mechanism and futuristic needs, Fuel Process. Technol. 71 (2001) 157–166.

[60] B.H. Davis, Fischer–Tropsch synthesis: reaction mechanisms for iron catalysts, Catal. Today 141 (2009) 25–33.

[61] Y. Pei, J. Liu, Y. Zhao, Y. Ding, T. Liu, W. Dong, H. Zhu, H. Su, L. Yan, J. Li, W. Li, High alcohols synthesis via Fischer–Tropsch reaction at cobalt metal/carbide interface, ACS Catal. 5 (2015) 3620–3624.

[62] Z. Zhao, W. Lu, R. Yang, H. Zhu, W. Dong, F. Sun, Z. Jiang, Y. Lyu, T. Liu, H. Du, Y. Ding, Insight into the formation of $Co@Co_2C$ catalysts for direct synthesis of higher alcohols and olefins from syngas, ACS Catal. 8 (2017) 228–241.

[63] J. Wei, Q. Ge, R. Yao, Z. Wen, C. Fang, L. Guo, H. Xu, J. Sun, Directly converting CO_2 into a gasoline fuel, Nat. Commun. 8 (2017) 15174.

[64] J. Wei, R. Yao, Q. Ge, Z. Wen, X. Ji, C. Fang, J. Zhang, H. Xu, J. Sun, Catalytic hydrogenation of CO_2 to isoparaffins over Fe-based multifunctional catalysts, ACS Catal. 8 (2018) 9958–9967.